Journal of
Water & Climate Change

A comparison of intense rainfall characteristics and mechanisms between monsoon onset and retreat over the Yangtze River Basin

Jiaxue Li[a,b], Yanjuan Wu [a,b,c,d,*], Cathryn Birch[c], Juliane Schwendike[c], Ailish Graham[c] and Gareth Berry[c]

[a] Department of Geography and Spatial Information Techniques, Ningbo University, Ningbo, Zhejiang 315211, China
[b] Ningbo Universities Collaborative Innovation Center for Land and Marine Spatial Utilization and Governance Research at Ningbo University, Ningbo 315211, China
[c] School of Earth and Environment, University of Leeds, Leeds LS2 9JT, UK
[d] Institute of East China Sea, Ningbo University, Ningbo 315211, China
*Corresponding author. E-mail: wuyanjuan@nbu.edu.cn

YW, 0000-0002-5208-1231

ABSTRACT

The thermodynamic and convective characteristics of the seasonal progression of the monsoon over eastern China are examined, with the aim of understanding why regional heavy rainfall events (RHREs) over the Yangtze River Basin (YRB) are more frequent and intense during the monsoon progression from mid-June to mid-July than during the retreat from mid-August to mid-September. During the monsoon progression, the southerly monsoon flow at low and mid-levels intensifies and moves northward, while the Western Pacific subtropical high shifts northeastward. These changes result in enhanced moisture advection over eastern China. The stronger southerly flow brings warmer and moist air into the YRB, leading to a higher equivalent potential temperature (θ_E) and favouring convection. Conversely, during the monsoon retreat, the northerly flow becomes stronger and drier, causing lower θ_E air over the YRB. Additionally, as the Western Pacific subtropical anticyclone retreats, easterly prevailing winds prevail over eastern China, causing reduced specific humidity. The monsoon progression period exhibits higher convective available potential energy but also higher convective inhibition, which is overcome by the presence of the monsoon front providing sufficient dynamical uplift. Understanding the severity of RHREs, particularly over the YRB, is crucial for improving forecasting capabilities and reducing societal vulnerability.

Key words: convective diagnostic, monsoon rainfall, RHREs, thermodynamical structure, YRB

HIGHLIGHTS

- Heavy rainfall events are more frequent and more intense during the progression of the monsoon rainy season than during its retreat over YRB.
- The frequency of occurrence and strength of the monsoon front is similar during monsoon progression and retreat.
- The southerly flow is stronger, and the equivalent potential temperature is higher during monsoon progression than during monsoon retreat.

GRAPHICAL ABSTRACT
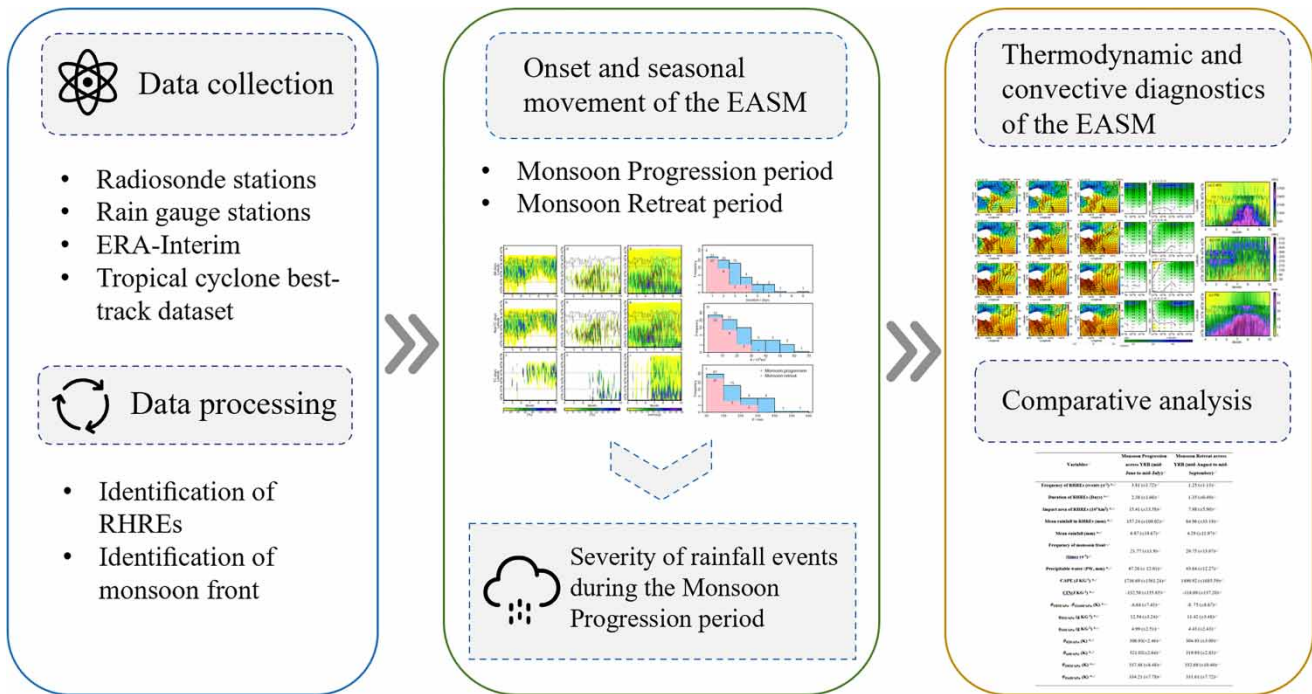
1. INTRODUCTION

Eastern China is the most important agricultural and industrial region in China. Rainfall is dominated by the East Asian Monsoon (EAM), which provides 70% of the annual rainfall (Wu *et al.* 2016a; Jin *et al.* 2024). The EAM is characterised by a distinct seasonal reversal of wind in the annual cycle, caused by the differential solar heating and thermal inertia of land and ocean (Ding 2007; Wu *et al.* 2023a). In summer, the temperature difference between land and ocean triggers the East Asian Summer Monsoon (EASM). The southerly monsoon flow within the EASM converges with a northerly flow, forming a subtropical monsoon front between eastern China and Japan (Fu & Qian 2015). Uplift and instabilities within the monsoon front, which is situated at the leading (northern) edge of the EASM, form the monsoon rain belt in the EASM (Wang *et al.* 2008, 2018). When the EASM and monsoon front advance northward, it can produce heavy rainfall and severe flooding. The dense population along eastern China, especially over the Yangtze River Basin (YRB), exasperates the human and financial cost of the floods (Wu *et al.* 2016a, 2023b). In the summer of 2020, the YRB experienced an anomalously long and persistent rainy season. Accumulated rainfall broke the historical record in 1961 and caused severe flooding with an estimated US $11.75 billion in economic losses (Ding *et al.* 2021; Wie *et al.* 2024). Conversely, when the monsoon front retreats back over the YRB region and western China between mid-August and mid-September, heavy rainfall and flooding are far less frequent (Ding 2007; Wu *et al.* 2019). Accurate monsoon rainfall predictions on both weather and climate timescales are imperative for flood disaster management and water resources planning, yet the location and intensity of the heaviest rainfall are poorly simulated by models (e.g. Chen & Bordoni 2014; Xin & Wang 2024). Therefore, there is an urgent need to understand the structural characteristics of the complex EASM, the dynamics of the monsoon front, and the associated large-scale circulations.

With the northward advance of the EASM, heavy rainfall occurs successively in different regions of China. In general, the climatological monsoon rain belt first appears in southern China around mid-May and remains there until mid-June, then migrates northward over the YRB and southern Japan between mid-June and mid-July. By mid-July the monsoon rain belt moves further north to northern China and Korea. From mid-August to mid-September the monsoon rain belt moves back to southern China (Wang & LinHo 2002; Ding 2007; Chen *et al.* 2021). During the retreat of the EASM, a sub-peak of rainfall occurs in West China, which features the last rainy season in China (Zhou & Wang 2019; Liu *et al.* 2023; Li & Zhu 2024). Luo *et al.* (2013) objectively define the onset and duration of the monsoon over southern China and the Yangtze-Huai River

basin and show that there are significant interannual variations in the timing of monsoon periods for both regions. The onset and cessation dates of the monsoon at each region are difficult to quantify, due to interannual variability, the variety of selected cases, data sources, time ranges, monsoon indices, and definitions of monsoon onset used in previous studies (Ding & Chan 2005). Thus, the monsoon rain belt, along with its associated heavy rainfall, exhibits significant interannual variability on both temporal and spatial scales, leading to the occurrence of floods and droughts in eastern China.

There have been several studies exploring the characteristics of monsoon rainfall in different regions of China. The majority of existing literature on EASM rainfall focuses on either the southern or central (YRB) regions of eastern China, as well as rainfall characteristics during the advance and retreat of the EASM (Wang & LinHo 2002; Zhu et al. 2008; Gao et al. 2011; Luo et al. 2013; Dong et al. 2022; Yao et al. 2022). Yao et al. (2022) examined the heavy rainfall in the YRB from June to July 2020 and found that there were 31,778 instances of short-duration heavy rainfall during this period, most of which were closely related to mesoscale convective systems. Luo et al. (2013) compared the characteristics of monsoon rainfall between South China and the YRB and found that the YRB had a higher contribution of heavy rainfall to the total monsoon rainfall. In almost all previous studies, heavy rainfall associated with the EASM is defined based on the daily/hourly rainfall total at individual points (station or grid value). One way to focus more on high-impact rainfall events is through the identification of regional heavy rainfall events (RHREs), which are characterised by their large spatial extent and long duration and often induce serious hydrological disasters with a substantial societal and economic impact. Wu et al. (2019) use an objective identification technique to identify RHREs from rain gauge observations during the summer monsoon season over eastern China and found that the seasonal variations of RHREs are highly associated with the movement of EASM.

The monsoon rain belt and its seasonal spatial distribution over eastern China are largely a result of the strength of the monsoon front and its location (Chen et al. 2006; Wie et al. 2024). The monsoon front over China is a unique subtropical moisture front in the lower troposphere, characterised by a strong moisture gradient (Ninomiya 1984; Fu & Qian 2015). Specifically, the monsoon front during the period of mid-June and mid-July can be identified as an area with strong equivalent potential temperature (Zhou et al. 2004; Li et al. 2018b) and saturation equivalent potential temperature gradients (Ding & Liu 2001), and a horizontal wind shear line (Akiyama 1973). The low-level convergence of the southerly monsoon flow with the northerly flow provides a mechanism for the uplift of moist monsoonal air, triggering deep convection along the front (Luo et al. 2014). The southerly or south-westerly low-level jet along the western rim of the Western Pacific subtropical high is one of the main components of EASM (Li & Zhu 2024). The jet transports warm and moist air from lower latitudes into the monsoon rain belt, leading to strong low-level convergence downstream of the jet core, and helping to establish an unstable atmosphere over eastern China (Li et al. 2018b). Thus, the onset and withdrawal of the EASM are closely related to the seasonal variation of the Western Pacific subtropical high. It controls the supply of lower-level moisture from the ocean to the land and determines the location where warm and moist oceanic air converges with the cold air from higher latitudes (Zhong et al. 2010; Ren et al. 2013; Liu et al. 2020; Yang et al. 2023). As the major monsoon rain belt is established over the YRB, the Western Pacific subtropical high moves northward with its zonal axis at 20°N–25°N (Zhong et al. 2010). The seasonal variation of the monsoon rain belt and heavy rainfall over eastern China is also under the influence of the migration of upper-level subtropical westerly jet cores over eastern China. Another reason for the formation of the monsoon rainfall over the YRB is the horizontal warm advection from the eastern flank of the Tibetan Plateau towards Japan by the upper westerly jet, which aids in inducing convection in the rain belt (Sampe & Xie 2010). Mesoscale features of the monsoon rain belt are also important for heavy rainfall, for example, a mesoscale vortex is found to be an important reason for the heavy rain over the YRB (Luo et al. 2020; Fu et al. 2021), but this is beyond the scope of this study.

The characteristics of RHREs over monsoon rain belts and their mechanisms have been studied on a case study or climatology basis. However, most of them focus on either the monsoon over southern China from mid-May to mid-June or over the YRB from mid-June to mid-July. In this study, characteristics of the entire seasonal progression and retreat of the EASM over the whole of eastern China are explored, including the monsoon front, the associated large-scale circulation, and thermodynamics, as well as RHRE. Most previous studies have been conducted using reanalysis products (Sampe & Xie 2010), multiple satellite products (Luo et al. 2013), and numerical simulations (Li et al. 2018a) that may not realistically reproduce reality. In this study, rain gauge and radiosonde observations, along with a quantitative climatology of the monsoon front are used to characterise the EASM progression and its associated RHREs.

The aim of this study is to explore why there are more frequent occurrences of RHREs during the onset of the monsoon season, when the front is over the YRB, than during the monsoon retreat, even though the monsoon front frequency and location are similar during both periods. Section 2 describes the dataset and methodology; Section 3 presents the onset

and seasonal movement of the monsoon front and associated rainfall; Section 4 and Section 5 present the thermodynamic perspectives and convective diagnostics across eastern China during the EASM; Section 6 presents a comparison between monsoon retreat and progression periods, followed by conclusions in Section 7.

2. DATA AND METHODS

2.1. Data

The Integrated Global Radiosonde Archive (IGRA) dataset from the National Oceanic and Atmospheric Administration (Durre *et al.* 2006, 2008; NOAA 2018) is used to analyse the thermodynamics of the onset and propagation of the EASM. A total of 171 radiosonde stations are located to the east of 100°E in mainland China and Mongolia (Figure 1, black crosses and red symbols). For this study, a 20-year time period from 1998 to 2017 was chosen to allow averaging of data over a sufficiently long period but within the limitations of the dataset lengths. In the region east of 100°E over mainland China and Mongolia, there are 15 radiosonde stations with at least 75% temporal coverage from 1998 to 2017 (Figure 1, red symbols), with soundings available daily at 0000 and 1,200 Coordinated Universal Time (UTC). Nine of these stations were selected for this study, based on data quality and distance from the meridional transect at 113°E (Figure 1, red circles and red line). The data are post-processed by linearly interpolating all sondes onto a standard set of 20 pressure levels (every 50 hPa from 100 to 1,000 hPa). Knowledge of the elevation of each station is provided within the IGRA dataset and is used to identify the pressure levels that are under the surface. Equivalent potential temperature (θ_E), saturated equivalent potential temperature (θ_{ES}), and specific humidity (q) were computed on the standard set of pressure levels during the post-processing.
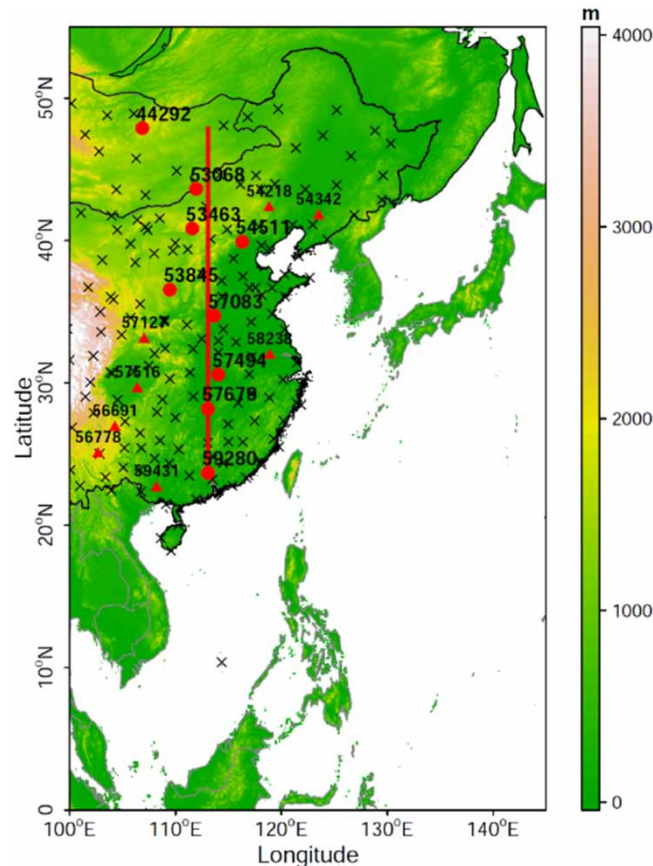

Figure 1 | All radiosondes launch locations in mainland China and Mongolia east of 100°E. Black crosses indicate the stations with poor-quality data, and red circles and triangles mark the stations with good-quality data. Red circles indicate the stations along a north–south transect (red line) selected in this study to characterise the thermodynamic structure of the EASM.

Daily rainfall from over 900 rain gauge stations throughout China is obtained from the National Meteorological Information Center of the China Meteorological Administration (NMIC/CMA) (CMA 2018). The dataset is subject to strict quality control procedures and has been used in numerous studies (e.g. Wu *et al.* 2016b, 2019). The rain gauge data are analysed over the same period as the radiosondes to identify the onset and progression of the monsoon rain belt and identify RHREs.

The European Centre for Medium-Range Weather Forecast reanalysis data (ERA-Interim) with a temporal resolution of 6 h and a horizontal resolution of 0.75° × 0.75° (Dee *et al.* 2011) from 1998 to 2017 is used to identify the monsoon front and examine changes in the large-scale circulations during the monsoon season over China.

Drivers of heavy rainfall over eastern China include both the EASM, which is the focus of this study, and landfalling tropical cyclones (TCs) (Wu *et al.* 2019; Liu *et al.* 2023). The TC best-track dataset from the China Meteorological Administration, spanning from 1949 to the present (Ying *et al.* 2014; CMA TC 2018), is used to identify landfalling TCs and assess their impact on the results. There is an average of 7.2 landfalling TCs per year during the monsoon season (April–September) between 1998 and 2017 over eastern China, and on average each TC lasts about 4 days. Most of the TCs make landfall on the southeastern coast of China from July to September. To avoid mixing the rainfall signal of the monsoon front and EASM with TCs, TC days are removed from most of the analysis.

2.2. Methods

2.2.1. Identification of RHREs

An objective identification technique for regional extreme events (Ren *et al.* 2012; Wu *et al.* 2019) is used to identify RHREs over eastern China using the rain gauge observations described above. This technique is based on three key steps. The first step is to define the stations with extreme rainfall using a threshold of 50 mm day^{-1}. The second step is to determine the daily RHREs, and the third step is to identify the temporal continuity of each daily RHRE between adjacent dates. This technique has been previously applied to identify RHREs and temperature extremes in China (Gong *et al.* 2012; Wang *et al.* 2014; Wu *et al.* 2019). Three RHRE indices are computed:

- *Duration* (*D*): The duration of each RHRE in a number of days.
- *Impact area* (*A*): Following the procedure of Wu *et al.* (2019), station data within an identified RHRE are first interpolated to a grid of 0.1° grid spacing. Within rolling window blocks of nine grid cells (spanning three rows and columns) centred on the grid cells containing stations of rainfall greater than 50 mm day^{-1}, grid cells of rainfall greater than 50 mm day^{-1} are then identified. This process is repeated for each day of the RHRE. The area covered by these identified grid cells is defined as the impact area (km^2).
- *Accumulated areal average rainfall depth* (*P*): For each day of an RHRE, the area-weighted average of rainfall for all affected grid cells is calculated. The average rainfall depth for each day of an RHRE is calculated from the corresponding affected grid cells using weights dependent on the area represented by the grid cell. The area of each grid cell is calculated according to the cosine of the latitude. *P* is the sum of the daily averaged rainfall depth during an RHRE (mm).

Further details of the technique for identifying RHREs can be found in Wu *et al.* (2019).

2.2.2. Identification of monsoon front

The position of the monsoon front is objectively identified based on boundaries in the wet bulb potential temperature (q_w) following the methods outlined in Hewson (1998) and Berry *et al.* (2011). The monsoon front was detected between May and September in the ERA-Interim reanalysis at 500 hPa for the period 1979–2013 in the region 0–60°N, 60–150°E. Due to the height terrain in the western part of the domain, 500 hPa was chosen rather than the more commonly used height of 850 hPa. The front positions are determined by joining grid boxes that contain front points on the basis of a maximum distance of 1.5° between adjacent front points. Only fronts exceeding 1,250 km in total length are retained. The locations of the objectively detected monsoon fronts are used in this study.

3. ONSET AND SEASONAL MOVEMENT OF THE EASM AND ASSOCIATED RAINFALL

The seasonal progression of the monsoon front is shown in latitude-time cross-sections of the normalised frequency of the monsoon front location in Figure 2(g). The band of latitudes over which the monsoon front is located ranges approximately from 25 to 40°N (Figure 2(a)). The monsoon front location varies on a daily basis due to synoptic variability. At the most
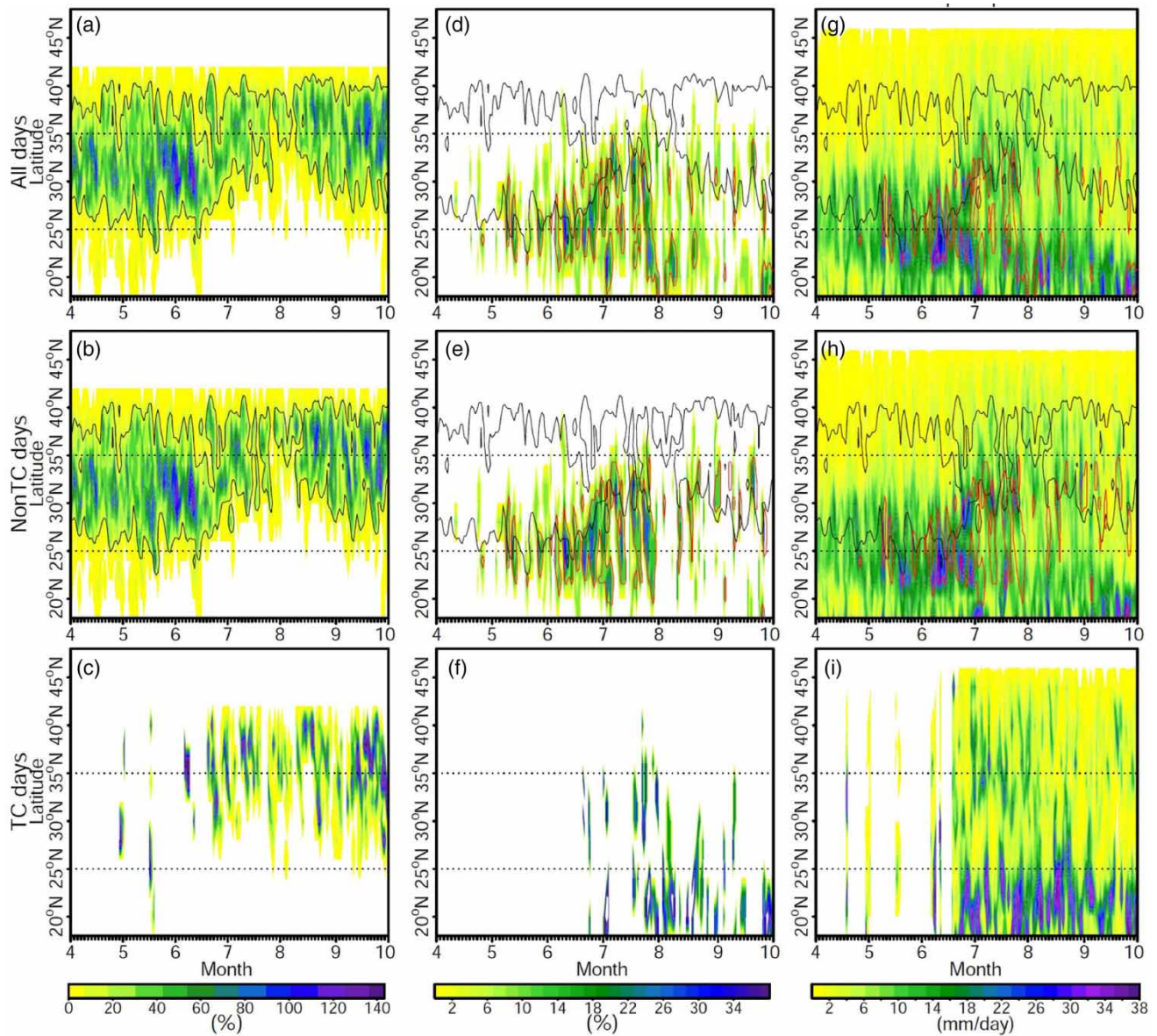
Figure 2 | Latitude-time Hovmöller plots of the frequency of monsoon front location (left), days of RHREs (middle), and daily mean rainfall (right), averaged over 110–115°E for April–September for all days (a, d, g), non-TC days (b, e, h), and TC days (c, f, i). All panels are normalised by the total number of days (a, d, g), the number of non-TC days (b, e, h), and the number of TC days (c, f, i). The two dashed lines mark the southerly and northerly boundaries of the YRB region, the black lines represent the contours at 15% of the normalised frequency of monsoon front location, and the red lines are the 7% contour of normalised RHRE days.

northern latitudes, the structure of the monsoon front is similar to that of a mid-latitude frontal system, which explains why fronts are identified around 40°N during all months between April and September. The region of frequently occurring monsoon fronts (frequency higher than 15%, in green) is between 26 and 40°N from May to mid-June. From mid-May onwards, the region with the majority of frequent occurrences of the monsoon front moves northwards, over the YRB, to 35°N between mid-June and the start of August. During early August, the fronts occur most frequently in northern China and Korea (i.e. north of 35°) (Lü *et al.* 2013). The southern extent of front occurrences starts to retreat southward from mid-August, reaching around 26°N by the end of September.

Monsoon front occurrences are associated with regions of heavy rainfall. The seasonal progression of RHRE days (Figure 2(d)) and the mean rainfall (Figure 2(g)) over eastern China broadly follow the seasonal progression of the southern

extent of the monsoon front. In April, before the onset of the summer monsoon over eastern China, the monsoon rain belt is observed between 23 and 30°N (i.e. to the south of the YRB) (Figure 2(g)) and is characterised by low-intensity rainfall and few RHREs (Figure 2(d)). The onset of the EASM in southern China (20 and 25°N) occurs with a steep rise in mean rainfall from early to mid-May, where the major rainfall belt remains until mid-June. During this time, RHREs occur frequently. From mid-June to mid-July, the latitude of the highest mean rainfall and the most RHREs advances northward, at the same time as the southern extent of monsoon front occurrences moves northward. This phase initiates the YRB monsoon rainy season in China and is called the 'Monsoon Progression' (mid-June to mid-July) period in this study. During this time, the monsoon front extends eastwards to the main islands of Japan, forming the Japanese Baiu rainy season (Ding & Chan 2005). From mid-July, the monsoon front progresses further northward over China, which produces a rainy season of about 1 month that is of lower intensity than in southern China and the Yangtze region. A decline in RHRE days is also observed. From mid-August to mid-September, the monsoon rain belt retreats southward to southern China, accompanied by the retreat of the southward extent of the monsoon front. This phase is called the 'Monsoon Retreat' (mid-August–mid-September) period in this study. During this time, another typical rainy season related to the retreat of EASM over western China and YRB is called the autumn rainy season in China (Zhou & Wang 2019). Over YRB, relatively low-intensity monsoon rainfall and a much smaller number of RHRE days are observed during the monsoon retreat period compared to the monsoon progression period, even though similarly frequent occurrences of the monsoon front occur.

Figure 2(b), 2(e), 2(h) and Figure 2(c), 2(f), 2(i) show the same as Figure 2(a), 2(d), and 2(g) but for non-TC days and TC days only, respectively. While non-TC days are similar to the results for all days (Figure 2(a), 2(d), and 2(g)), TC days indicate that TC rainfall mostly contributes to rainfall in southern China. During TC days, the number of RHREs and the mean rainfall are both much lower than those over eastern China within the monsoon front region on non-TC days. It should be noted, however, that the monsoon front positions and the related rainfall that occurs on days identified as having landfalling TCs (Figure 2(c), 2(f), and 2(i)) are not necessarily caused by the TCs themselves. This study aims to understand the role of the monsoon front in producing heavy rainfall. Given the possible influence of landfalling TCs on our results, for the remainder of the paper, the results are only shown for non-TC days (Figure 2(b), 2(e), and 2(h)).

There is a higher frequency of longer-duration, larger-area, higher rainfall intensity events during the monsoon progression period than during the monsoon retreat period (Figure 3). These events occur rarely but have a significant impact on the risk of severe floods and socio-economic impacts. On average, 3.81 events occur every year during the monsoon progression period, but only 1.25 events occur during the monsoon retreat period (Table 1). Events during the monsoon progression period have a mean duration of 2.38 days compared to 1.35 days during the monsoon retreat period, a mean impact area of 15.41×10^4 km^2 compared to 7.98×10^4 km^2, and a mean accumulated areal average rainfall depth of 157.24 mm compared to 84.96 mm (Table 1). The difference between the averages of RHREs indices in each period is significant at the 0.01 level for all three characteristics using the student's t-test. In general, RHREs are significantly more intense during the monsoon progression period than during the monsoon retreat period. This could lead to extensive agricultural destruction, disruptions to food security, and significant economic losses (Lee *et al.* 2024). In addition, urban areas may experience overwhelmed drainage systems, leading to infrastructure damage and potential public health crises with the more severe RHREs during the monsoon progression period. Understanding these patterns and their mechanisms is of critical importance for effective risk management and reduction.

4. THERMODYNAMICAL STRUCTURE OF THE EASM

4.1. Prior to monsoon onset (April to mid-May)

Prior to the monsoon onset (April to mid-May), there are south-westerly winds at 850 hPa over southern China, caused by the westerly jet over Eurasia to the southern edge of the Tibetan Plateau, which converges with the easterly trade winds (Figure 4(a)–4(c)). This strong low-level south-westerly jet is attributed to the mechanical and thermal effects of the Tibetan Plateau (Wang *et al.* 2009), which is the direct climatic cause of the persistent spring rains in southern China (Tian & Yasunari 1998). At the same time, the Western Pacific subtropical high still prevails in the South China Sea, and an easterly dry flow dominates there. Along the meridional transect, regions south of 35°N experience weak easterly flow below 800 hPa (Figure 5(a)–5(c)). Above 800 hPa the flow is westerly, with a maximum between 300 and 100 hPa and 28–31°N associated with the subtropical jet. The highest velocities in the jet occur in early April, and then the jet begins to migrate northward and weakens from mid-April to mid-May. The distribution of the meridional wind exhibits a strong North–South divide, with
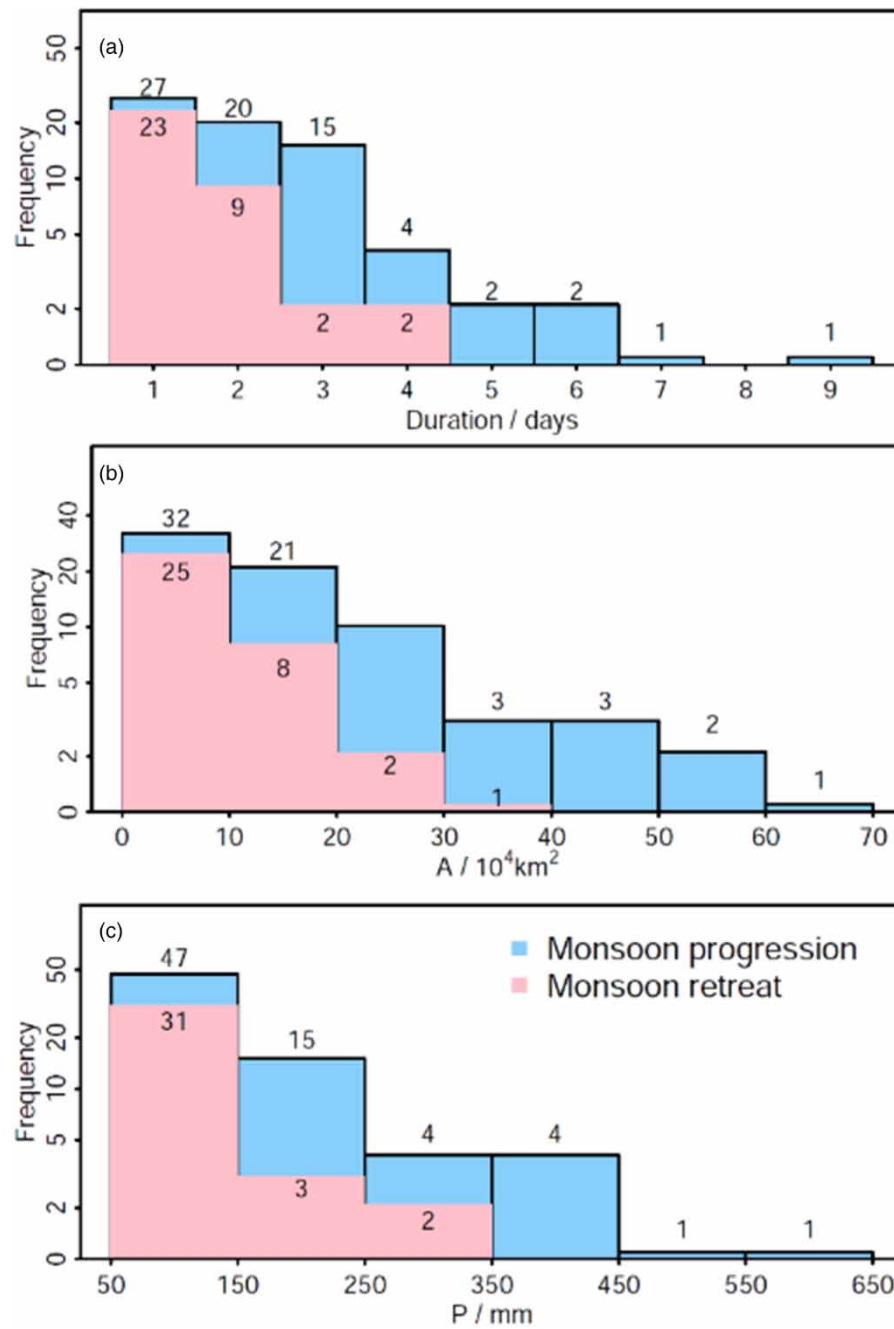
Figure 3 | Distribution of the frequency of RHREs over the YRB during the monsoon progression (mid-June to mid-July) and monsoon retreat (mid-August to mid-September) periods on a logarithmic scale for (a) duration (D), (b) impact area (A), and (c) accumulated rainfall amount (P).

southerlies between 25 and 30°N and northerlies further north throughout the depth of the troposphere (Figure 6(a)–6(c)). This dry and cold northerly flow originates from the westerly flow along the north side of the Tibetan Plateau. The convergence of tropical air from the south with drier, poleward air at 30°N causes persistent spring rainfall in southern China. It should be noted that the magnitude of the zonal wind is much greater than that of the meridional wind, signalling that the flow in the mid and upper levels is dominated by the presence of the subtropical jet.

A deep moist layer (relative humidity >80%, 1,000–700 hPa) is present in the transect south of 28°N (Figure 7(a)–7(c)). This moist layer, which results from the dominance of southerly winds transporting moisture from the tropics, supports the

Table 1 | Average and standard deviation (in brackets) of RHREs and variables characterising the monsoon conditions for the radiosonde stations located over the Yangtze River Basin (YRB) during the monsoon progression (mid-June to mid-July), and monsoon retreat (mid-August to mid-September) periods

Variables	Monsoon progression across YRB (mid-June to mid-July)	Monsoon retreat across YRB (mid-August to mid-September)
Frequency of RHREs (events year^{-1})*	3.81 ($\pm$ 1.72)	1.25 ($\pm$ 1.13)
Duration of RHREs (days)*	2.38 ($\pm$ 1.60)	1.35 ($\pm$ 0.49)
Impact area of RHREs (10^4 km^2)*	15.41 ($\pm$ 13.58)	7.98 ($\pm$ 5.90)
Mean rainfall in RHREs (mm)*	157.24 ($\pm$ 109.02)	84.96 ($\pm$ 33.19)
Mean rainfall (mm)*	6.87 ($\pm$ 18.67)	4.29 ($\pm$ 11.97)
Frequency of monsoon front (times year^{-1})	21.77 ($\pm$ 11.9)	20.75 ($\pm$ 13.07)
PW (mm)*	47.26 ($\pm$ 12.01)	43.64 ($\pm$ 12.27)
CAPE (J kg^{-1})*	1,736.69 ($\pm$ 1,561.24)	1,490.92 ($\pm$ 1,685.59)
CIN(J kg^{-1})*	-132.50 ($\pm$ 155.85)	-116.09 ($\pm$ 137.20)
$\theta_{E850 \text{ hPa}} - \theta_{ES600 \text{ hPa}}$ (K)*	-6.64 ($\pm$ 7.43)	-8.75 (± 8.67)
$q_{850 \text{ hPa}}$ (g kg^{-1})*	12.54 ($\pm$ 3.24)	11.42 ($\pm$ 3.48)
$q_{600 \text{ hPa}}$ (g kg^{-1})*	4.99 ($\pm$ 2.51)	4.43 ($\pm$ 2.43)
$\theta_{850 \text{ hPa}}$ (K)*	306.93($+$ 2.46)	304.93 ($\pm$ 3.09)
$\theta_{600 \text{ hPa}}$ (K)*	321.02($\pm$ 2.64)	319.89 ($\pm$ 2.83)
$\theta_{E850 \text{ hPa}}$ (K)*	337.48 ($\pm$ 8.48)	332.69 ($\pm$ 10.40)
$\theta_{E600 \text{ hPa}}$ (K)*	334.21 ($\pm$ 7.78)	331.61 ($\pm$ 7.72)

* indicates that the difference between the average of each variable in the two periods significant at the 0.01 level by student's t-test.

persistent spring rainfall. Further north, the air in the northerlies is much drier. The equivalent potential temperature (θ_E) is a measure of both temperature and humidity in the vertical profile and is an indicator of convective potential. Before mid-May, there is a north–south gradient in θ_E, but low values dominate at low and mid-levels along the entire transect (Figure 8(a)–8(c)). The lower θ_E values in the north indicate colder, drier air from higher latitudes and the higher values of θ_E in the south indicate the southern flow of moist, warm air from the tropics.

4.2. Monsoon onset over southern China (mid-May to mid-June)

Mid-May sees the onset of the monsoon in southern China. Westerly monsoonal flow originating from the equatorial Indian Ocean and the Bay of Bengal associated with the Somali jet intensifies and expands eastward into the South China Sea (Figure 4(c) and 4(d)) at the same time as the north-eastward shift in the Western Pacific subtropical high takes place (not shown). The south-westerly monsoon flow from the equatorial Indian Ocean and the Bay of Bengal is moister than the westerly flow originating from the southern edge of the Tibetan Plateau (Figure 4). A large-scale low-level anticyclonic circulation associated with Western Pacific subtropical high dominates in the tropical Western Pacific. This circulation features prevailing southeasterlies from the tropical Western Pacific to Southern China at 850 hPa. The warm and moist southerly flow brings abundant water vapour to southern China, contributing to the monsoon onset in southern China. Chow et al. (2007) and Simmonds et al. (1999) indicated the water vapour that supports the summer rainfall over southern China comes mainly from the South China Sea originating from the equatorial Indian Ocean, the Bay of Bengal, and the Western Pacific Ocean.

During the mid-May to mid-June period, low-level (1,000–900 hPa) zonal wind (Figure 5(d) and 5(e)) is still weak and largely unchanged compared to the previous month. At upper levels, the maximum velocity of the subtropical jet decreases to 35 m s^{-1} by late June, causing the gradient in wind speed between the upper and mid-levels to decrease. The horizontal extent of the jet also decreases during this time, with the southernmost extent of the core migrating north from 25 to 28°N. The moist southerly monsoon flow dominates the lower and mid-levels in the regions south of 27°N during this period, and these southerlies extend to 40°N below 800 hPa by the end of June (Figure 6(d) and 6(e)). At mid-levels, the wind north of 27°N remains northerly, causing an intrusion of dry and cold northerly air from northern China (Figure 6(d) and 6(e)) that likely acts as a
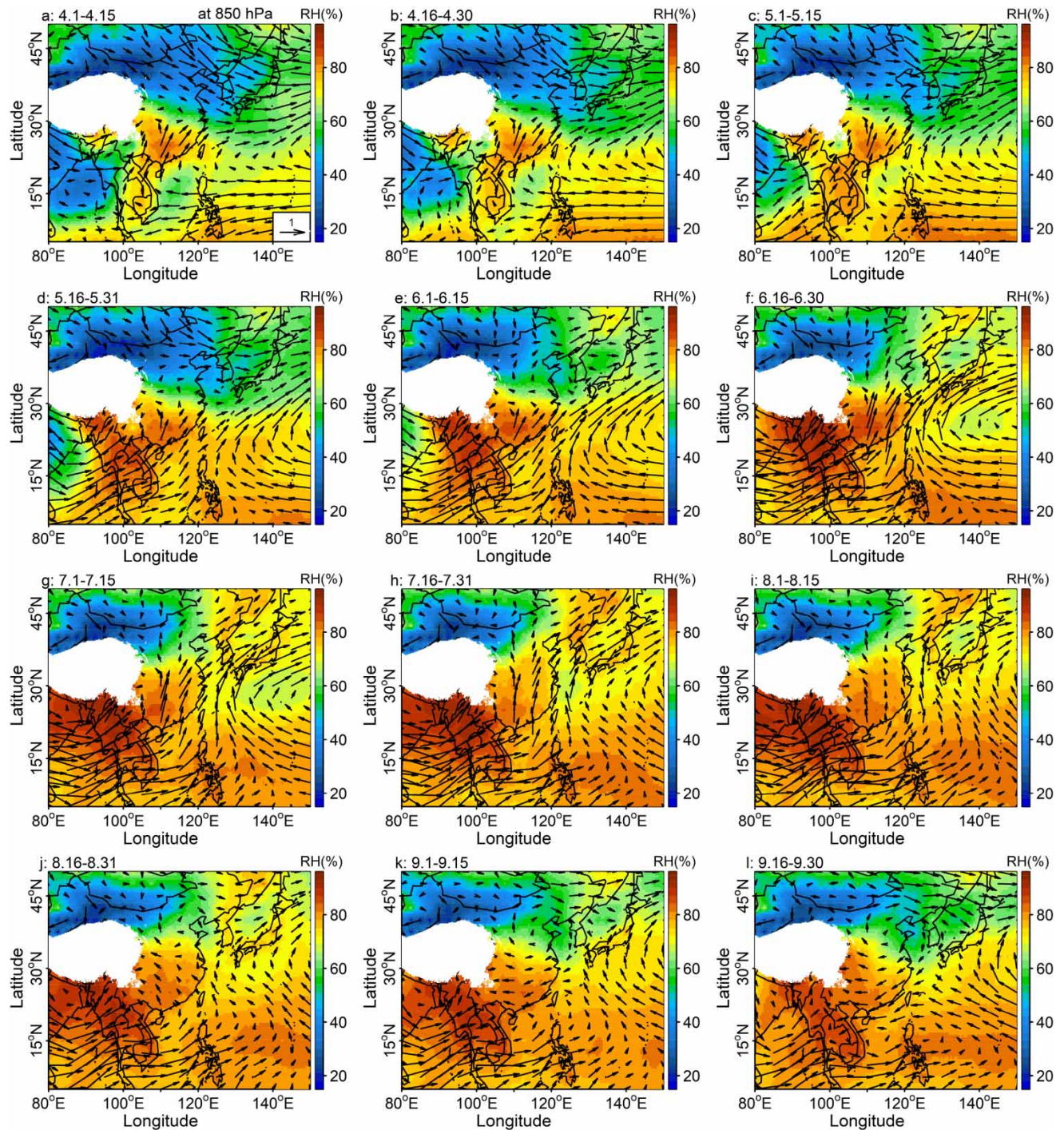
Figure 4 | Mean ERA-Interim relative humidity (%, shaded) and horizontal wind (m s^{-1}, arrows) at 850 hPa for every half month from April to September between 1998 and 2017. White regions indicate areas where the pressure level is below the orography.

cap and suppresses moist convection, in a similar way to over India in the early monsoon season (Parker *et al.* 2016). Therefore, the northern limit of the monsoon rain belt is located to the south of this mid-level dry air. At the same time, increases in moisture from the surface to 200 hPa in the troposphere occur in the south (Figure 7(d) and 7(e)), characterised by the vertical extension of the high relative humidity in the south half of the domain region. An increase in θ_E values along the transect at lower and mid-levels occurs during the southern China pre-monsoon season (Figure 8(d) and 8(e)). This observed increase in
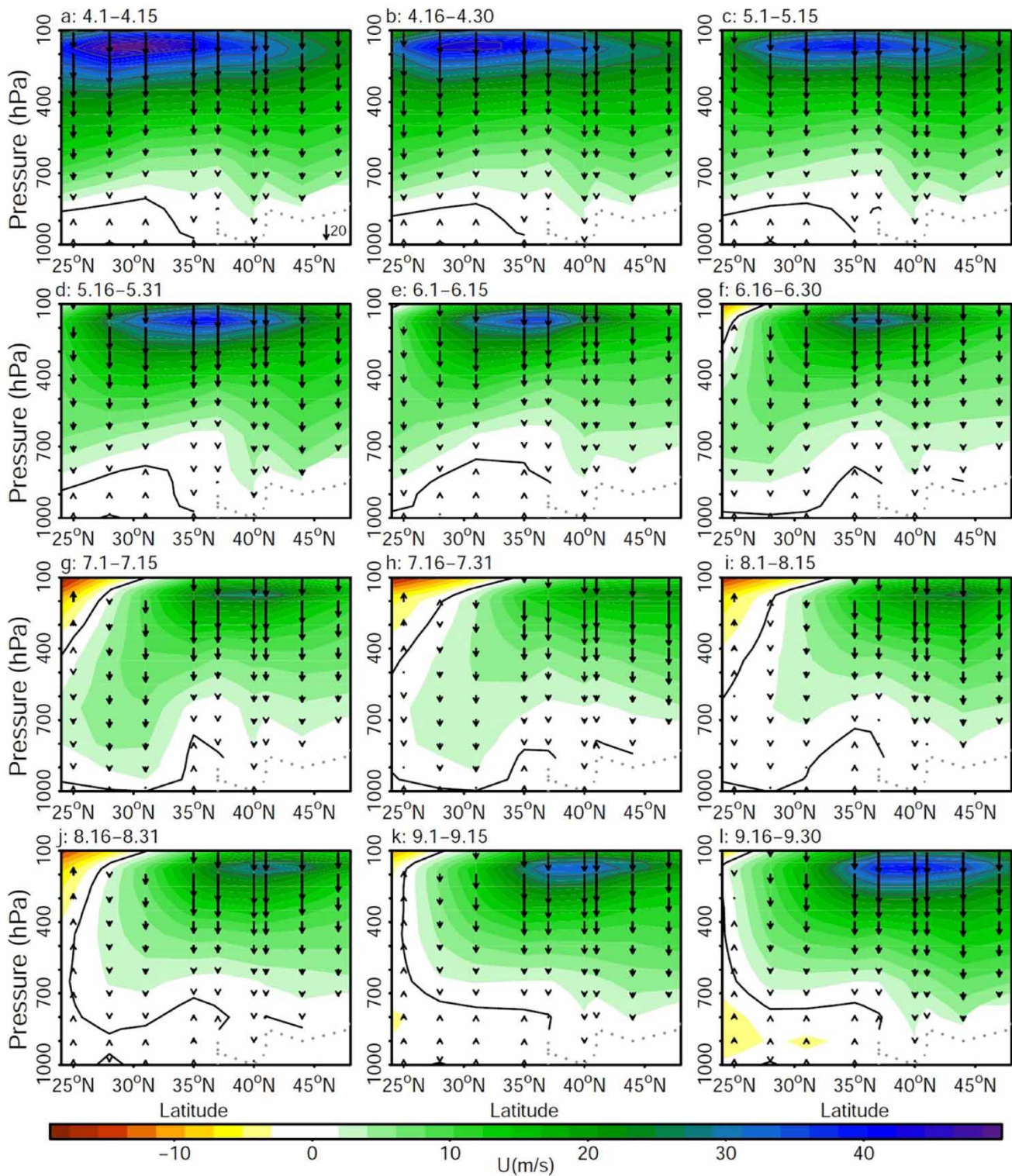
Figure 5 | Meridional transects of zonal wind (shading and arrows, m s^{-1}) from radiosonde data averaged between 1998 and 2017 for days without landfalling TCs for: (a) 1–15 April, (b) 16–30 April, (c) 1–15 May, (d) 16–31 May, (e) 1–15 June, (f) 16–30 June, (g) 1– 15 July, (h) 16–31 July, (i) 1–15 August, (j) 16–31 August, (k) 1–15 September, and (l) 16–30 September. The zero-value zonal wind is marked by the solid black contour. Positive zonal wind values (westerly flow) are displayed in green and blue, and negative values (easterly flow) in yellow. The orography surface is marked by the dotted grey line.
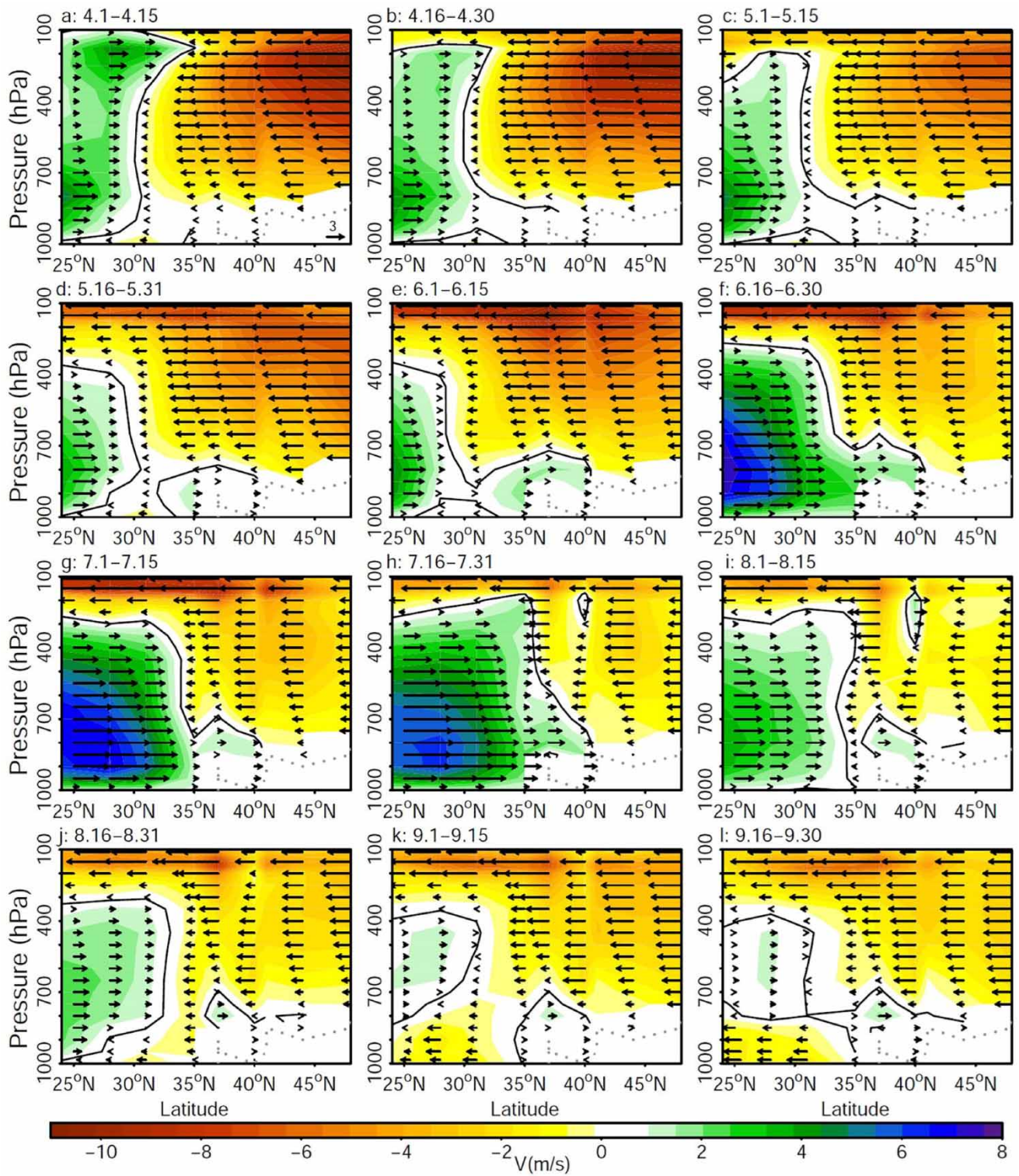
Figure 6 | Same as Figure 6, but for the meridional wind. Positive meridional wind values (southerly flow) are shown in green and blue, and negative values (northerly flow) are shown in yellow and red.
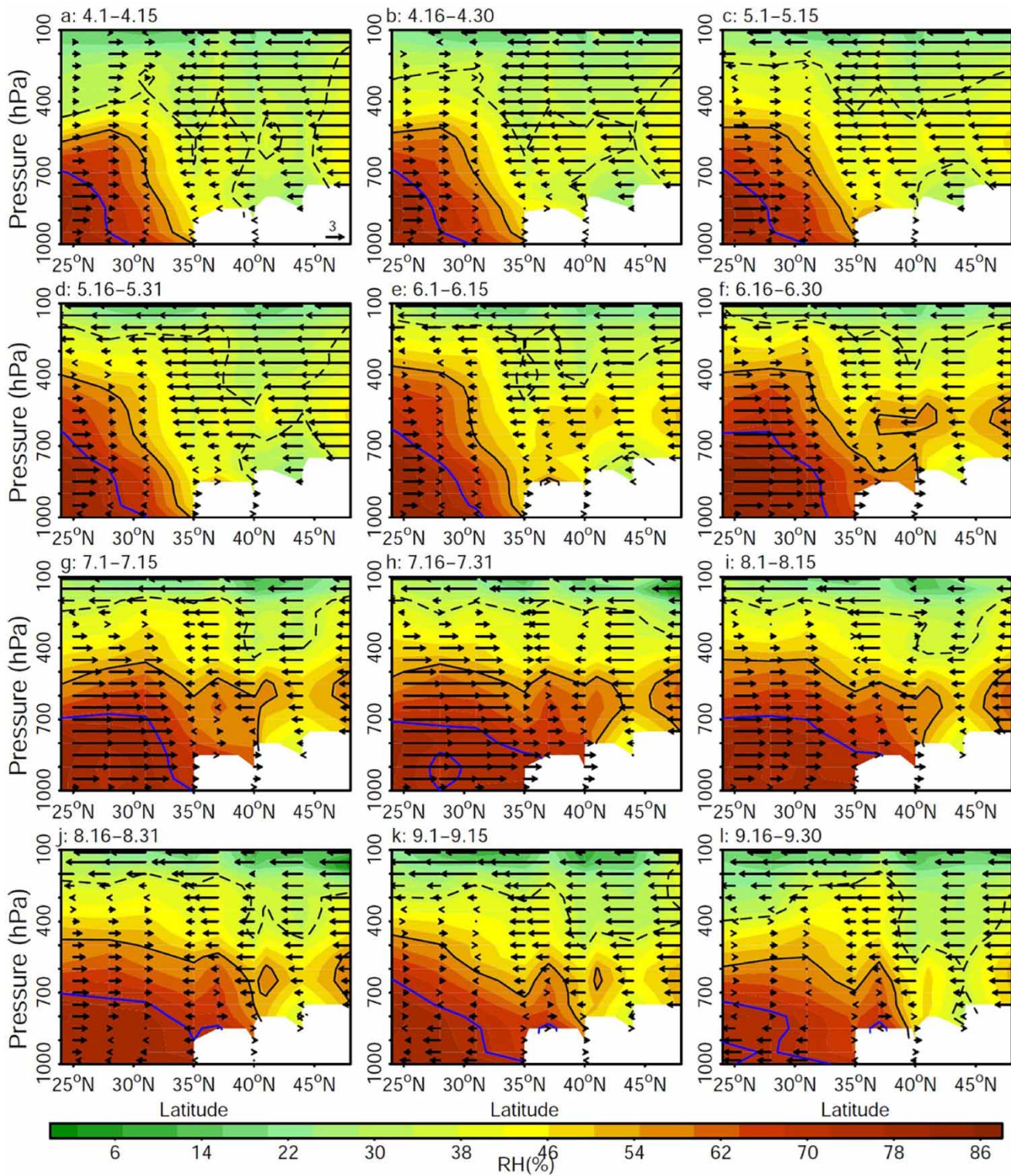
Figure 7 | Same as Figure 6, but shading represents relative humidity (%). The solid blue, solid black, and dashed black lines indicate the relative humidity at 80, 65, and 50%, respectively. The arrows show the meridional wind (m s⁻¹).
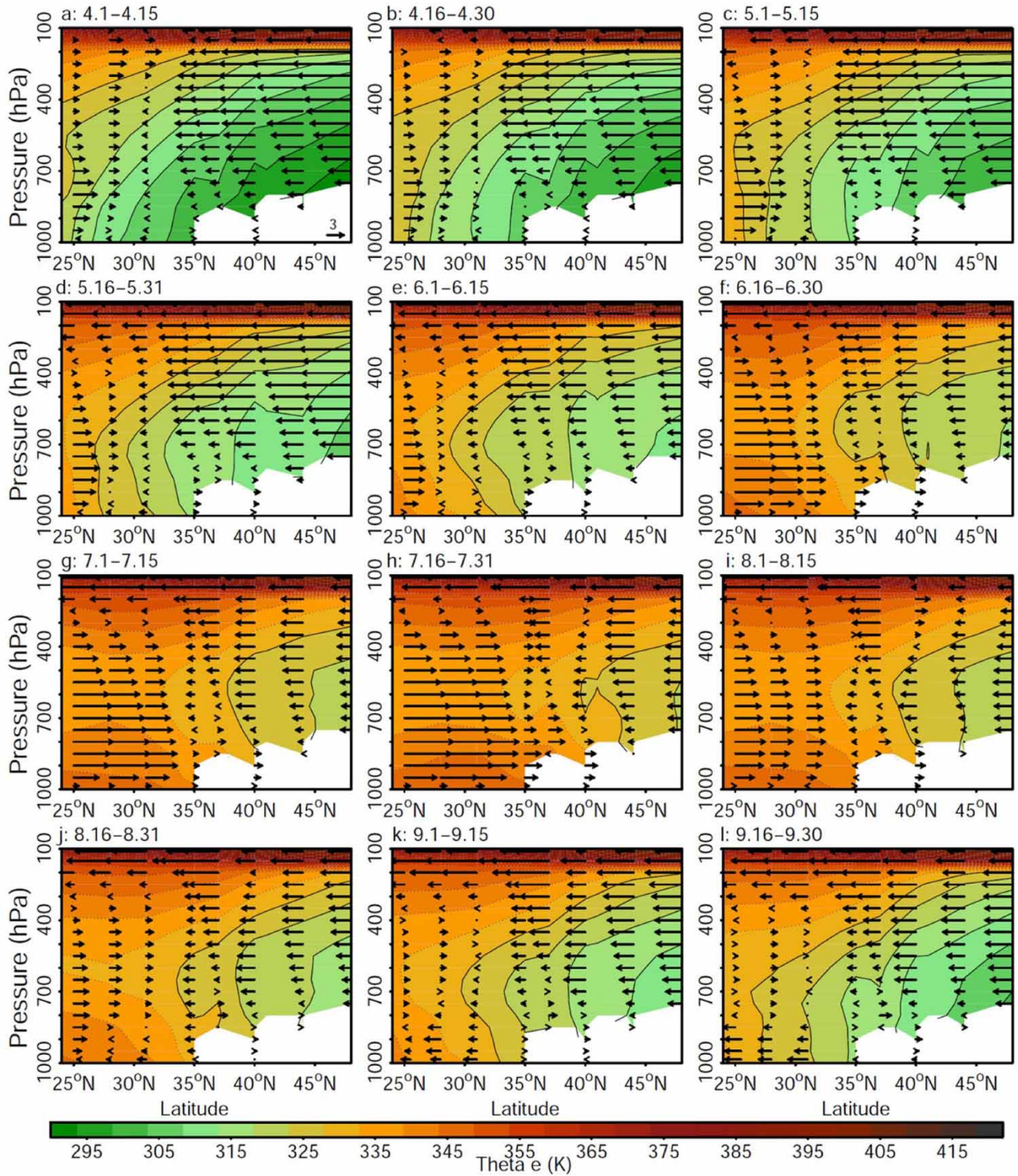
Figure 8 | Same as Figure 6, but for equivalent potential temperature (θ_E, K). Dashed lines represent values above 335 K and solid lines indicate values below this threshold. The arrows show the meridional wind (m s^{-1}).

θ_E in the south is much higher below 700 hPa due to the low-level monsoon flow from the south and the intrusion of mid-level dry and cold northerly air from the north. The strong gradient of θ_E with height leads to the presence of potential instability in southern China (Trachte & Bendix 2012). This unstable condition may become conditionally unstable if the air is lifted and becomes saturated.

4.3. Monsoon progression across the YRB (mid-June to mid-July)

The monsoon migrates northward over the YRB between mid-June and mid-July with the continued north-eastward shift and strengthening of the Western Pacific subtropical high. Between mid-June and mid-July the high pressure in the western Pacific is at its maximum causing anticyclonic circulation over the coastal region of East China, with easterlies south of 25°N and westerlies north of 30°N (Figure 4(f) and 4(g)). This kind of anticyclonic circulation pattern usually tends to result in heavier rainfall in the YRB through the strengthened convergence of tropical air flow with mid-latitude northerly air (Lau et al. 2000; Zhou & Yu 2005; Zhou et al. 2009). The south-easterly flow related to this anticyclonic circulation transports moisture from the West Pacific to the YRB and supports the onset of the monsoon there. In addition, another branch of moisture transport to this region is given by the south-westerly monsoon flow from the equatorial Indian Ocean and the Bay of Bengal. Zhou et al. (2010) indicate that both moisture sources reach their maximum in July. Thus, they contribute to the high intensity of the mean rainfall and more severe RHREs over the YRB during the monsoon progression season.

Between mid-June and mid-July, the westerly winds extend towards the surface (800–950 hPa) in regions south of 30°N (Figure 5(f) and 5(g)), which acts to weaken and subsequently block the low-level easterlies. At upper levels, the continued northward migration and weakening of the subtropical jet core occurs. The jet core moves northwards to around 35°N and its maximum velocity decreases to 28 m s^{-1}. As the monsoon progresses, the continued acceleration and northward progression of the southerly monsoon flow is apparent (Figure 6(f) and 6(g)), transporting large amounts of moisture into the YRB until mid-July. The intrusion of mid-level dry, cold northerly flow retreats northward to 35°N, and these mid-level northerlies become confined to altitudes above 700 hPa.

Along with the acceleration and northward movement of the southerly flow, the moistening of the troposphere from the surface to 200 hPa continues (Figure 7(f) and 7(g)). The increase in θ_E keeps extending further north to the YRB at lower and mid-levels until mid-July, which indicates the northward expansion and the acceleration of southerlies (Figure 8(f) and 8(g)). It is notable that sharp vertical gradients in θ_E at low levels occur south of the monsoon rain belt, but that the vertical θ_E gradient remains nearly constant at mid-levels. The potential instability under 700 hPa extends to the YRB.

4.4. Monsoon in northern China (mid-July to mid-August)

As the season of the monsoon progression across YRB comes to an end, the monsoon continues to migrate northward to northern China. The onset of the monsoon in Northern China is signalled by the north-eastward shift of the anticyclonic circulation (Figure 4(h) and 4(i)). The south-easterly flow along the western rim of the Western Pacific subtropical high from the subtropical Western Pacific transports moisture to northern China. The enhanced south-westerly flow also brings water vapour over this region from the South China Sea. The northward long-distance moisture transport over southern China and the YRB to northern China is vital for the onset of the monsoon in northern China (Sun et al. 2007). Thus, only sufficiently strong northward moisture transport associated with the EASM leads to favourable conditions for heavy rainfall in northern China.

From mid-July to mid-August, at upper levels, the subtropical jet reaches its maximum northward location of approximately 42°N and the wind speed at the 200-hPa jet core reduces to 22 m s^{-1} (Figure 5(h) and 5(i)). The northward expansion and acceleration of the southerlies in the southern part of the transect continued during this period. They reach a maximum northward location of about 37°N at mid and upper levels and vertically extend to 200 hPa (Figure 6(h) and 6(i)). Northerlies still dominate in the north but weaken at all levels of the troposphere.

At the same time, moistening of the troposphere at lower and mid-levels continues and higher relative humidity regions extend further north to approximately 40°N by mid-August (black line, Figure 7(h) and 7(i)). The high θ_E region below 700 hPa extends northward up to about 40°N (Figure 8(h) and 8(i)). As the northern China monsoon onset occurs the entire region from 24 to 40°N becomes potentially unstable with a decrease of θ_E with height up to ~700 hPa. The decrease in the meridional gradient of θ_E from mid-May to mid-August indicates the northward advance of the monsoon.

4.5. Monsoon retreat across the YRB (mid-August to mid-September)

As the monsoon season in northern China comes to an end, the monsoon starts to retreat southward from mid-August to mid-September. The withdrawal of the EASM is indicated by the south-eastward retreat of the Western Pacific subtropical high, and by the resulting prevailing easterlies over eastern China between 20 and 40°N, where previously the prevailing wind direction was southerly at 850 hPa (Figure 4(j)–4(l)). This change in wind direction corresponds to the rapid westward retreat of the south-westerly flow.

During the monsoon retreat period, the subtropical jet starts to shift southward and strengthens (Figure 5(j)–5(l)). The northerlies strengthen at all levels in the troposphere and begin to migrate southward (Figure 6(j)–6(l)). At the same time, the southerly winds that previously dominated the troposphere in the south of the transect weaken in both velocity, and the vertical and horizontal extent of the southerlies are confined to the region south of 30°N between 800 and 400 hPa, and the maximum velocity of the southerlies decreases to about 1 m s^{-1} by late September.

There is a decrease in relative humidity in the regions north of 35°N at all levels (Figure 7(j)–7(l)), which results from the strengthening of the northerly flow. In the regions south of 35°N, a deep moist layer (relative humidity >80%, 1,000–700 hPa) is still present, although the relative humidity decreases at upper levels. This moisture south of 35°N is transported by the easterly flow from the East China Sea during the monsoon retreat. A decrease in θ_E along the transect below 200 hPa occurs during the monsoon retreat (Figure 8(j)–8(l)), which is a result of the southward retreat of the monsoon and the strengthening of the cold and dry northerly flow. An increase in the meridional gradient of θ_E during this period is also observed.

5. CONVECTIVE DIAGNOSTICS

The previous section illustrated the vertical and meridional thermodynamical structure of the atmosphere during the progression and retreat of the EASM. In this section, the likelihood for convection along the meridional transect is considered, using convective available potential energy (CAPE), convective inhibition (CIN), and precipitable water (PW) derived from the radiosonde observations (Figure 9).

Prior to the monsoon onset (April to mid-May), CAPE is relatively weak and CIN is high north of about 27°N along the meridional transect. PW is relatively low apart from in the very south. Low CAPE and high CIN are indicators of suppressed convection. CAPE values to the south of 27°N increase during the monsoon onset in southern China from below 1,000 J kg^{-1} in mid-May to approximately 2,000 J kg^{-1} by mid-June, indicating a higher potential for intense convective activity. In contrast, CAPE to the north of 27°N remains weak until mid-June. High CIN values in YRB (−114 J kg^{-1}) and north China (−195 J kg^{-1}) persist during the monsoon onset in southern China. At the same time, high PW values progress northward at a steady rate throughout May to June, with the highest values observed in southern China providing favourable conditions for convection in the south. This behaviour is concurrent with the observed high frequency of RHREs and the southward extent of monsoon front locations in southern China during this time (red and black contours in Figure 9, respectively).

During the season of Monsoon Progression across the YRB (mid-June to mid-July), CAPE increases along the transect. South of 27°N, CAPE increases from approximately 2,000 to >2,700 J kg^{-1}. The largest increase in CAPE occurs over the YRB, from relatively weak values below 900 J kg^{-1} to values of 2,000–2,700 J kg^{-1} by mid-July. CAPE to the north of 35°N slightly increases but remains lower than further south. Accompanying the increase in CAPE in the YRB is a large decrease in CIN (−105 J kg^{-1}). The magnitude of CIN in regions north of 35°N is still large (−185 J kg^{-1}) and an increase in PW to more than 39 mm over the YRB occurs. The change towards favourable conditions for convection over the YRB indicates a high likelihood of deep convection, which is reflected in the northward progression of RHREs and the southern extent of the monsoon front position over the YRB.

The magnitudes of CAPE, CIN, and PW change considerably during the onset of the monsoon in northern China (mid-June to mid-August). North of 35–40°N, CAPE increases from moderate values of ~900 to ~1,500 J kg^{-1}, the average magnitude of CIN decreases to ~160 J kg^{-1}, and PW increases to more than 39 mm. In northern China, both CAPE and PW reach their maximum values as the monsoon onset occurs, although their values are not as large as those in the YRB and southern China. The combination of moderate CAPE and high CIN cannot support intense convection in this region, thus even though the monsoon front is present, the number of RHRE days and the intensity of the monsoon rainfall in northern China remains low compared to that further south.
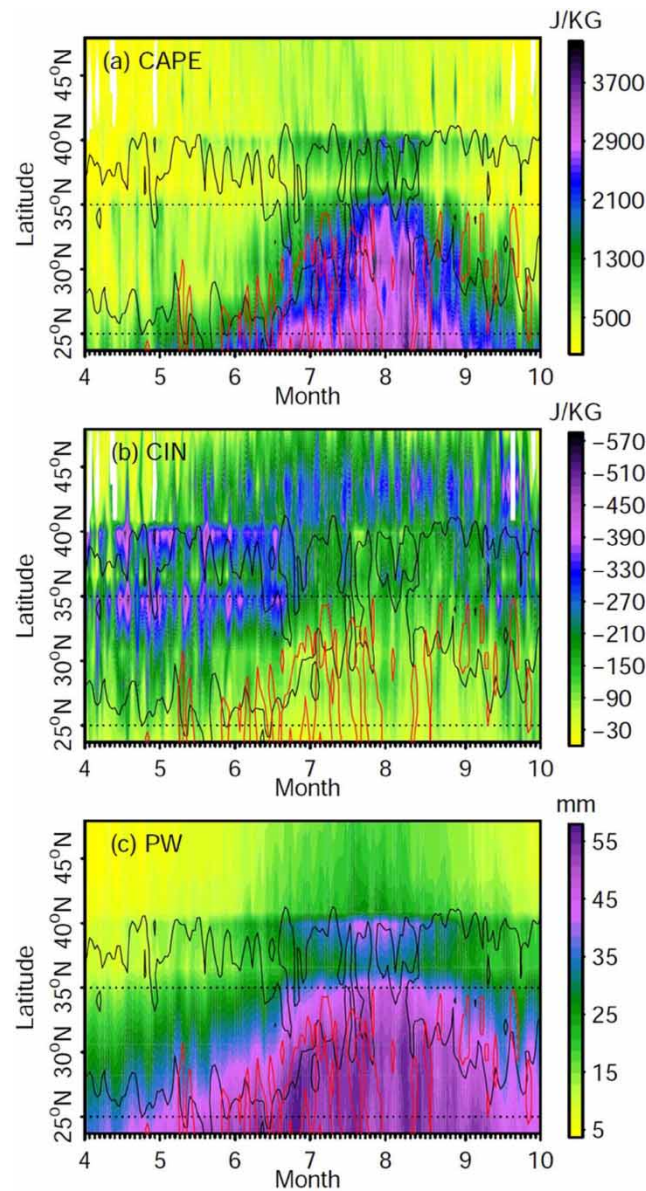
Figure 9 | Latitude-time sections along the radiosonde transect averaged over 110–115°E for April–September 1998 and 2017 for days without landfalling TCs, (a) CAPE, (b) CIN, and (c) PW. The black lines are the 15% contours for the normalised frequency of the monsoon front location. The red lines are the 7% contour of normalised days of RHREs. The dotted black horizontal lines mark the southerly and northerly boundaries of the YRB region.

The Monsoon Retreat period occurs between mid-August and mid-September. The region of high CAPE retreats towards the south and larger magnitude CIN returns. The southern extent of the monsoon front occurrences moves southward and the number of normalised RHRE days reduces to less than 7% (red contour in Figure 2). There is a large asymmetry in the number of RHRE days over the YRB in mid-June to mid-July compared with mid-August to mid-September, even though the location and frequency of the monsoon front are similar in both periods.

6. COMPARISON BETWEEN THE MONSOON RETREAT AND PROGRESSION PERIODS

In this section, the state of the atmosphere over the YRB during the Monsoon Progression (mid-June to mid-July) and Monsoon Retreat (mid-August to mid-September) periods is compared. The aim is to understand why Relative Humidity and Rainfall Extremes (RHREs) occur frequently in the Monsoon Progression period but are much more limited in number in

the Monsoon Retreat period, even though the monsoon front frequency and location are similar in both seasons. A summary of key convective indicators between the two periods, averaged over the radiosonde stations, is compared (Table 1). The difference between the average diagnostics in the two periods is significant at the 0.01 level using the Student's t-test for all diagnostics apart from the frequency of monsoon fronts (stars, Table 1).

Mean rainfall over the YRB is 6.87 mm day^{-1} during the Monsoon Progression compared with 4.29 mm day^{-1} during the Monsoon Retreat. RHREs are more frequent, longer in duration, larger in the impact area, and have a larger amount of rainfall in the Monsoon Progression period compared to the Monsoon Retreat period. The frequency of the identified monsoon front occurrences is 21.77 times year^{-1} during the Monsoon Progression compared to 20.75 times year^{-1} during the Monsoon Retreat, and the difference between them is not statistically significant. This result and the plots of the monsoon front frequency in Figure 2(a)–2(c) suggest that the presence of the monsoon front is similar in both periods.

The south-westerly flow brings warmer, moister air to the YRB region during the Monsoon Progression period, which is indicated by statistically significant higher specific humidity (q) and θ_E values in the Monsoon Progression period at both 850 and 600 hPa with 12.54 g KG^{-1} for q_{850hPa}, 4.99 g KG^{-1} for q_{600hPa}, 337.48 K for $\theta_{E850hPa}$ and 334.21 K for $\theta_{ES600hPa}$. During the Monsoon Retreat period, prevailing north-easterly or easterly at low-level transports cold air to the YRB region, which results in lower specific humidity (q) and θ_E values (11.42 g KG^{-1} for q_{850hPa}, 4.43 g KG^{-1} for q_{600hPa}, 332.69 K for $\theta_{E850hPa}$ and 331.61 K for $\theta_{ES600hPa}$). In addition, the Monsoon Progression period experiences more surface heating through higher solar radiation due to longer days and the sun being more directly overhead compared to the Monsoon Retreat period, which helps to maintain the warmer low-level temperatures in the Monsoon Progression period.

Both PW and CAPE, indicators of a higher likelihood of convection, are higher in the Monsoon Progression than in the Monsoon Retreat period, although the standard deviation in CAPE is large. CIN is of a larger magnitude during the Monsoon Progression period, which suggests a greater barrier to convection. It is likely that the instabilities in the monsoon front are able to overcome the high CIN values. $\theta_{E850hPa} - \theta_{ES600hPa}$ is a measure of the stability of the profile, where positive values indicate unstable profiles with a high potential for convection. The mean value is negative in both periods (the standard deviations are similar), but the values in the Monsoon Progression period are closer to zero than in the Monsoon Retreat period, suggesting less stable profiles on average.

In summary, the period of the Monsoon Progression over the YRB is warmer, more humid, and more unstable than during the Monsoon Retreat. The location and frequency of the monsoon front, and the instabilities it provides, are similar in both periods. The difference in the state of the atmosphere between both periods produces a higher number of larger, more intense RHREs in the YRB in mid-June to mid-July (Monsoon Progression) compared with mid-August to mid-September (Monsoon Retreat).

7. CONCLUSIONS

The monsoon front at the leading edge of the EASM produces a region of uplift and instability, leading to heavy rainfall over eastern China. In this study, monsoon fronts were identified up to 40°N in all months from April to September. The southern boundary of the monsoon front progresses northwards over the YRB from mid-June to mid-July (Monsoon Progression period) and retreats back over the YRB between mid-August and mid-September (Monsoon Retreat period). The location and frequency of the monsoon front are fairly similar during both periods. However, there is a higher frequency of longer-duration, larger-area, higher intensity RHRE events during the Monsoon Progression period than the Monsoon Retreat period over the YRB. A 20-year climatology of radiosonde profiles and convective diagnostics over a north–south transect across China at approximately 110°E is used to characterise the progression and retreat of the EASM and understand why there is such a difference in extreme rainfall characteristics between the two seasons.

The radiosonde climatology shows that throughout all stages of the EASM progression, the changing balance between the warm, moist southerly monsoonal flow and the cold, dry northerly flow is important for the formation of intense rainfall, especially at mid-levels. The northward progression of the monsoon flow, along with the continued north-eastward shift of the Western Pacific subtropical high, which causes the advection of moisture from the South China Sea and western Pacific into eastern China, drives increases in θ_E and the associated monsoon rainfall. The convective diagnostics along the meridional transect show that, throughout all stages of the seasonal progression of the EASM, the northern limit of the monsoon rain belt is located to the south of the mid-level dry air, where the magnitude of CIN is sufficiently low and CAPE and PW are sufficiently high for convection to occur. As the monsoon retreats southward from mid-August, a decrease in θ_E values

and moisture along the entire transect is evident, indicating the strengthening and southward shift of the cold, dry northerly flow and retreat of the warm, moist southerly flow. At the same time, the south-eastward retreat of the Western Pacific sub-tropical high results in easterly prevailing winds over eastern China. The dominance of northerly and easterly flow at low levels over eastern China indicates the withdrawal of the EASM.

The southerly monsoon flow is stronger at low and mid-levels during the Monsoon Progression period than the Monsoon Retreat period, which brings higher temperatures and more moisture into the YRB. Stronger surface heating in June/July compared to August/September, combined with the advection of warmer, moister air, causes low and mid-level θ_E to be higher in the monsoon progression than monsoon retreat period, producing more RHREs. The atmosphere is also less stable in the monsoon progression period, with larger CAPE values. CIN is larger in magnitude in the monsoon progression period than in the monsoon retreat period, but it is likely that the presence of the monsoon front provides sufficient uplift to overcome this. This study advances our understanding of the EASM system and how intense rainfall is produced, particularly in the YRB region, which is especially prone to severe flooding events. This type of process understanding is critical for improving the representation of severe weather in weather and climate models, and thus, for improving our ability to forecast them on a range of timescales and reducing their societal impact.

ACKNOWLEDGEMENTS

DATA AVAILABILITY STATEMENT

All relevant data are included in the paper or its Supplementary Information.

CONFLICT OF INTEREST

The authors declare there is no conflict.

REFERENCES

Akiyama, T. 1973 The large-scale aspects of the characteristics of the Baiu front. *Papers in Meteorology and Geophysics* **24** (2), 157–188. https://doi.org/10.2467/mripapers1950.24.2_157.

Berry, G. J., Reeder, M. J. & Jakob, C. 2011 A global climatology of atmospheric fronts. *Geophysical Research Letters* **38** (4), L04809-1–L04809-5. https://doi.org/10.1029/2010GL046451.

Chen, J. & Bordoni, S. 2014 Intermodel spread of East Asian summer monsoon simulations in CMIP5. *Geophysical Research Letters* **41** (4), 1314–1321. https://doi.org/10.1002/2013GL058981.

Chen, G. T. J., Wang, C. C. & Lin, L. F. 2006 A diagnostic study of a retreating Mei-Yu front and the accompanying low-level jet formation and intensification. *Monthly Weather Review* **134** (3), 874–896. https://doi.org/10.1175/MWR3099.1.

Chen, G. X., Du, Y. & Wen, Z. P. 2021 Seasonal, interannual, and interdecadal variations of the East Asian summer monsoon: A diurnal-cycle perspective. *Journal of Climate* **34** (11), 4403–4421. https://doi.org/10.1175/JCLI-D-20-0882.1.

Chow, K. C., Tong, H. W. & Chan, J. C. L. 2007 Water vapor sources associated with the early summer precipitation over China. *Climate Dynamics* **30** (5), 497–517. https://doi.org/10.1007/s00382-007-0301-6.

CMA 2018 *Daily Surface Climate Variables of China From V3.0 Data*. NMIC/CMA. Available from: http://data.cma.cn/data/cdcdetail/dataCode/SURF_CLI_CHN_MUL_DAY_V3.0.html (accessed 1 June 2018).

CMA TC 2018 *CMA TC Best-Track Dataset*. CMA. Available from: tcdata.typhoon.org.cn (accessed 1 June 2018).

Dee, D. P., Uppala, S. M., Simmons, A. J., Berrisford, P., Poli, P., Kobayashi, S., Andrae, U., Balmaseda, M. A., Balsamo, G., Bauer, D. P. & Bechtold, P. 2011 The ERA-Interim reanalysis: Configuration and performance of the data assimilation system. *Quarterly Journal of the Royal Meteorological Society* **137** (656), 553–597. https://doi.org/10.1002/qj.828.

Ding, Y. H. 2007 The variability of the Asian summer monsoon. *Journal of the Meteorological Society of Japan, Ser II* **85**, 21–54. https://doi.org/10.2151/jmsj.85B.21.

Ding, Y. H. & Liu, Y. J. 2001 Onset and the evolution of the summer monsoon over the South China Sea during SCSMEX field experiment in 1998. *Journal of the Meteorological Society of Japan* **79** (1B), 255–276. https://doi.org/10.2151/jmsj.79.255.

Ding, Y. H. & Chan, J. C. 2005 The East Asian summer monsoon: An overview. *Meteorology and Atmospheric Physics* **89** (1–4), 117–142. https://doi.org/10.1007/s00703-005-0125-z.

Ding, Y. H., Liu, Y. J. & Hu, Z. Z. 2021 The record-breaking Mei-yu in 2020 and associated atmospheric circulation and tropical SST anomalies. *Advances in Atmospheric Sciences* **38** (12), 1–14. https://doi.org/10.1007/S00376-021-0361-2.

Dong, G., Jiang, Z., Wang, Y., Tian, Z. & Liu, J. 2022 Evaluation of extreme precipitation in the Yangtze River Delta Region of China using a 1.5 km mesh convection-permitting regional climate model. *Climate Dynamics* **59** (7–8), 2257–2273. https://doi.org/10.1007/s00382-022-06208-1.

Durre, I., Vose, R. S. & Wuertz, D. B. 2006 Overview of the integrated global radiosonde archive. *Journal of Climate* **19** (1), 53–68. https://doi.org/10.1175/JCLI3594.1.

Durre, I., Vose, R. S. & Wuertz, D. B. 2008 Robust automated quality assurance of radiosonde temperatures. *Journal of Applied Meteorology and Climatology* **47** (8), 2081–2095. https://doi.org/10.1175/2008JAMC1809.1.

Fu, J. L. & Qian, W. H. 2015 The structure of a typical Mei-Yu front identified by the equivalent temperature. *Atmospheric and Oceanic Science Letters* **4** (2), 109–113. https://doi.org/11446913.

Fu, S. M., Tang, H., Li, Y., Ma, H. & Sun, J. H. 2021 On the relationship of a low-level jet and the formation of a heavy-rainfall-producing mesoscale vortex over the Yangtze River Basin. *Atmosphere* **2** (12), 156. https://doi.org/10.3390/atmos12020156.

Gao, H., Yang, S., Kumar, A., Hu, Z. Z., Huang, B., Li, Y. & Jha, B. 2011 Variations of the East Asian Mei-Yu and simulation and prediction by the NCEP Climate Forecast System. *Journal of Climate* **24** (1), 94–108. https://doi.org/10.1175/2010JCLI3540.1.

Gong, Z., Wang, X., Cui, D., Wang, Y., Ren, F., Feng, G., Zhang, Q., Zou, X. & Wang, X. 2012 The identification and changing characteristics of regional low temperature extreme events. *Journal of Applied Meteorological Science* **23** (2), 195–204. https://doi.org/10.1007/s11783-011-0280-z.

Hewson, T. D. 1998 Objective fronts. *Meteorological Applications* **5** (1), 37–65. https://doi.org/10.1017/S1350482798000553.

Jin, D. C., Huo, L. W., Yan, Z., Luo, J. J. & Wang, Z. Q. 2024 Enhanced influence of tropical Atlantic Sea surface temperature anomalies on east Asian summer monsoon since the late 1970s. *Climate Dynamics* 1–13. https://doi.org/10.1007/s00382-024-07173-7.

Lau, K. M., Kim, K. M. & Yang, S. 2000 Dynamical and boundary forcing characteristics of regional components of the Asian summer monsoon. *Journal of Climate* **13** (14), 2461–2482. https://doi.org/10.1175/1520-0442(2000)013 < 2461:DABFCO > 2.0.CO;2.

Lee, C. C., Zeng, M. & Luo, K. 2024 How does climate change affect food security? Evidence from China. *Environmental Impact Assessment Review* **104**, 107324. https://doi.org/10.1016/j.eiar.2023.107324.

Li, X. J. & Zhu, B. Q. 2024 Interaction between the westerlies and Asian monsoons in the middle latitudes of China: Review and prospect. *Atmosphere* **15** (3), 274. https://doi.org/10.3390/atmos15030274.

Li, H., Hu, Y., Zhou, Z., Peng, J. & Xu, X. 2018a Characteristic features of the evolution of a Meiyu frontal rainstorm with Doppler radar data assimilation. *Advances in Meteorology* **2018** (3), 1–17. https://doi.org/10.1155/2018/9802360.

Li, Y., Deng, Y., Yang, S. & Zhang, H. 2018b Multi-scale temporospatial variability of the East Asian Meiyu-Baiu fronts: Characterization with a suite of new objective indices. *Climate Dynamics* **51** (5–6), 1659–1670. https://doi.org/10.1007/s00382-017-3975-4.

Liu, B. Q., Yan, Y. H., Zhu, C. W., Ma, S. M. & Li, J. Y. 2020 Record-breaking Meiyu rainfall around the Yangtze River in 2020 regulated by the subseasonal phase transition of the North Atlantic Oscillation. *Journal of Geophysical Research-Atmospheres* **47** (22), 1–8. https://doi.org/10.1029/2020GL090342.

Liu, Y. L., Sun, X. G. & Yang, X. Q. 2023 Stage-dependent influence of PDO on interdecadal summer precipitation anomalies in eastern China. *Climate Dynamics* **61** (5), 2071–2084. https://doi.org/10.1007/s00382-023-06667-0.

Lü, J. M., Ju, J. H. & Tao, S. Y. 2013 Re-discussion on East Asian Meiyu rainy season. *Atmospheric and Oceanic Science Letters* **6** (5), 279–283. https://doi.org/11447094.

Luo, Y., Wang, H., Zhang, R., Qian, W. & Luo, Z. 2013 Comparison of rainfall characteristics and convective properties of monsoon precipitation systems over South China and the Yangtze and Huai River basin. *Journal of Climate* **26** (1), 110–132. https://doi.org/10.1175/JCLI-D-12-00100.1.

Luo, Y., Gong, Y. & Zhang, D. L. 2014 Initiation and organizational modes of an extreme-rain-producing mesoscale convective system along a Mei-Yu Front in East China. *Monthly Weather Review* **142** (1), 203–221. https://doi.org/10.1175/MWR-D-13-00111.1.

Luo, Y. L., Sun, J. S., Li, Y., Xia, R. D., Du, Y., Yang, S., Zhang, Y. C., Chen, J., Dai, K., Shen, X., Chen, H. M., Zhou, F. F., Liu, Y. M., Fu, S. M., Wu, M. W., Xiao, T. G., Chen, Y. R. X., Li, H. Q. & Li, M. X. 2020 Science and prediction of heavy rainfall over China: Research progress since the reform and opening-up of the People's Republic of China (in Chinese). *Acta Meteorologica Sinica* **78** (3), 419–450. https://doi.org/10.1007/s13351-020-0006-x.

Ninomiya, K. 1984 Characteristics of Baiu front as a predominant subtropical front in the summer northern hemisphere. *Journal of the Meteorological Society of Japan* **62** (6), 880–894. https://doi.org/10.2151/jmsj1965.62.6_880.

NOAA 2018 *Derived-v2 Parameters Computed From v1.20 Data*. NOAA/Integrated Global Radiosonde Archive. Available from: ftp://ftp.ncdc.noaa.gov/pub/data/igra/derived/derived-por/. (accessed 1 June 2018).

Parker, D. J., Willetts, P., Birch, C., Turner, A. G., Marsham, J. H., Taylor, C. M., Kolusu, S. & Martin, G. M. 2016 The interaction of moist convection and mid-level dry air in the advance of the onset of the Indian monsoon. *Quarterly Journal of the Royal Meteorological Society* **142** (699), 2256–2272. https://doi.org/10.1002/qj.2815.

Ren, F. M., Cui, D., Gong, Z., Wang, Y., Zou, X., Li, Y., Wang, S. & Wang, X. 2012 An objective identification technique for regional extreme events. *Journal of Climate* **25** (20), 7015–7027. https://doi.org/10.1175/JCLI-D-11-00489.1.

Ren, X., Yang, X. Q. & Sun, X. 2013 Zonal oscillation of western Pacific subtropical high and subseasonal SST variations during Yangtze persistent heavy rainfall events. *Journal of Climate* **26** (22), 8929–8946. https://doi.org/10.1175/JCLI-D-12-00861.1.

Sampe, T. & Xie, S. P. 2010 Large-scale dynamics of the Meiyu–Baiu rainband: Environmental forcing by the westerly jet. *Journal of Climate* **23** (1), 113–134. https://doi.org/10.1175/2009JCLI3128.1.

Simmonds, I., Bi, D. & Hope, P. 1999 Atmospheric water vapor flux and its association with rainfall over China in summer. *Journal of Climate* **12** (5), 1353–1367. https://doi.org/10.1175/1520-0442(1999)012 < 1353:AWVFAI > 2.0.CO;2.

Sun, L., Shen, B., Gao, Z., Sui, B., Bai, L., Wang, S. H., Gang, A. & Li, J. 2007 The impacts of moisture transport of East Asian monsoon on summer precipitation in Northeast China. *Advances in Atmospheric Sciences* **24** (4), 606–618. https://doi.org/10.1007/s00376-007-0606-8.

Tian, S. F. & Yasunari, T. 1998 Climatological aspects and mechanism of spring persistent rains over central China. *Journal of the Meteorological Society of Japan* **76** (1), 57–71. https://doi.org/10.2151/jmsj1965.76.1_57.

Trachte, K. & Bendix, J. 2012 Katabatic flows and their relation to the formation of convective clouds – idealized case studies. *Journal of Applied Meteorology and Climatology* **51** (8), 1531–1546. https://doi.org/10.1175/JAMC-D-11-0184.1.

Wang, B. & LinHo. 2002 Rainy season of the Asian–Pacific summer monsoon. *Journal of Climate* **15** (4), 386–398. https://doi.org/10.1175/1520-0442(2002)015 < 0386:RSOTAP > 2.0.CO;2.

Wang, B., Wu, Z., Li, J., Liu, J., Chang, C. P., Ding, Y. & Wu, G. 2008 How to measure the strength of the East Asian summer monsoon. *Journal of Climate* **21** (17), 4449–4463. https://doi.org/10.1175/2008JCLI2183.1.

Wang, R. J., Zhao, B. K. & Wu, G. X. 2009 New evidences on the climatic causes of the formation of the spring persistent rains over southeastern China. *Advances in Atmospheric Sciences* **26** (6), 1081–1087. https://doi.org/10.1007/s00376-009-7202-z.

Wang, Y., Ren, F. M. & Zhang, X. 2014 Spatial and temporal variations of regional high temperature events in China. *International Journal of Climatology* **34** (10), 3054–3065. https://doi.org/10.1002/joc.3893.

Wang, Y., Zhang, L., Peng, J. & Guan, J. 2018 Mesoscale gravity waves in the Mei-Yu front system. *Journal of the Atmospheric Sciences* **75** (2), 587–609. https://doi.org/10.1175/JAS-D-17-0012.1.

Wie, J., Kang, J. & Moon, B. K. 2024 Role of Madden–Julian Oscillation in predicting the 2020 East Asian summer precipitation in subseasonal-to-seasonal models. *Scientific Reports* **14** (1), 865. https://doi.org/10.1038/s41598-024-51506-9.

Wu, Y. J., Wu, S. Y., Wen, J. H., Tagle, F., Xu, M. & Tan, J. G. 2016a Future changes in mean and extreme monsoon precipitation in the middle and lower Yangtze River Basin, China, in the CMIP5 models. *Journal of Hydrometeorology* **17** (11), 2785–2797. https://doi.org/10.1175/JHM-D-16-0033.1.

Wu, Y. J., Wu, S. Y., Wen, J. H., Xu, M. & Tan, J. G. 2016b Changing characteristics of precipitation in China during 1960–2012. *International Journal of Climatology* **36** (3), 1387–1402. https://doi.org/10.1002/joc.4432.

Wu, Y. J., Ji, H. X., Wen, J. H., Wu, S. Y., Xu, M., Tagle, F., He, B., Duan, W. L. & Li, J. X. 2019 The characteristics of regional heavy precipitation events over eastern monsoon China during 1960–2013. *Global and Planetary Change* **172**, 414–427. https://doi.org/10.1016/j.gloplacha.2018.11.001.

Wu, R., Chen, G. X. & Luo, Z. J. 2023a Strong coupling in diurnal variations of clouds, radiation, winds, and precipitation during the East Asian summer monsoon. *Journal of Climate* **36** (5), 1347–1368. https://doi.org/10.1175/JCLI-D-22-0330.1.

Wu, X. J., Wang, L., Niu, Z., Jiang, W. X. & Cao, Q. 2023b More extreme precipitation over the Yangtze River Basin, China: Insights from historical and projected perspectives. *Atmospheric Research* **292**, 106883. https://doi.org/10.1016/j.atmosres.2023.106883.

Xin, F. & Wang, W. 2024 Extended-range forecast of winter rainfall in the Yangtze River Delta based on intra-seasonal oscillation of atmospheric circulations. *Atmosphere* **15** (2), 206. https://doi.org/10.3390/atmos15020206.

Yang, K., Liu, C. L., Cai, J. X., Cao, N., Liao, X. Q., Su, Q. Y., Jin, L., Zheng, R., Zhang, Q. K. & Wang, L. 2023 The north-south shift of ridge location of the western Pacific subtropical high and its influence on the July precipitation in Jianghuai region 1978–2021. *Frontiers in Earth Science* **11**, 1251294. https://doi.org/10.3389/feart.2023.1251294.

Yao, X., Zhang, H., Ma, J., Shi, D., Wang, W. & Wang, G. 2022 Characteristics of newly formed mesoscale convective systems during the abnormal precipitation over the Yangtze River basin from June to July, 2020. *Atmospheric Science Letters* **23** (10), e1114. https://doi.org/10.1002/asl.1114.

Ying, M., Zhang, W., Yu, H., Lu, X., Feng, J., Fan, Y., Zhu, Y. & Chen, D. 2014 An overview of the China Meteorological Administration tropical cyclone database. *Journal of Atmospheric and Oceanic Technology* **31** (2), 287–301. https://doi.org/10.1175/JTECH-D-12-00119.1.

Zhong, Z., Wang, X. & Min, J. 2010 Testing the influence of western Pacific subtropical high. *Theoretical and Applied Climatology* **100** (1–2), 67–78. https://doi.org/10.1007/s00704-009-0166-1.

Zhou, T. J. & Yu, R. C. 2005 Atmospheric water vapor transport associated with typical anomalous summer rainfall patterns in China. *Journal of Geophysical Research-Atmospheres* **110** (D8). https://doi.org/10.1029/2004JD005413.

Zhou, B. & Wang, Z. 2019 Enlightenment from heavy autumn rain of West China in 2017: Synergic role of atmospheric circulation at mid-high latitudes and oceanic background. *Theoretical and Applied Climatology* **138** (1–2), 263–274. https://doi.org/10.1007/s00704-019-02809-9.

Zhou, Y., Gao, S. & Shen, S. S. 2004 A diagnostic study of formation and structures of the Meiyu front system over East Asia. *Journal of the Meteorological Society of Japan* **82** (6), 1565–1576. https://doi.org/10.2151/jmsj.82.1565.

Zhou, T., Gong, D., Li, J. & Li, B. 2009 Detecting and understanding the multi-decadal variability of the East Asian Summer Monsoon – recent progress and state of affairs. *Meteorologische Zeitschrift* **18** (4), 455–467. https://doi.org/10.1127/0941-2948/2009/0396.

Zhou, X. X., Ding, Y. H. & Wang, P. X. 2010 Moisture transport in the Asian summer monsoon region and its relationship with summer precipitation in China. *Journal of Meteorological Research* **24** (1), 31–42. Available from: http://jmr.cmsjournal.net/en/article/id/1231.

Zhu, X., Wu, Z. & He, J. 2008 Anomalous Meiyu onset averaged over the Yangtze River valley. *Theoretical and Applied Climatology* **94** (1–2), 81–95. https://doi.org/10.1007/s00704-007-0347-8.